1B.3 ESTIMATING RADAR WIND OBSERVATION ERROR AND NCEP WRF BACKGROUND WIND ERROR COVARIANCES FROM RADAR RADIAL-VELOCITY INNOVATIONS

Qin Xu[1]*, Kang Nai[2], Li Wei[2], Huijuan Lu[2], Pengfei Zhang [2], Shun Liu[3], and David Parrish[3]

[1]NOAA/National Severe Storms Laboratory, Norman, Oklahoma
[2]Cooperative Institute for Mesoscale Meteorological Studies, University of Oklahoma
[3]NOAA/NCEP, Camp Springs, MD

1. INTRODUCTION

In three-dimensional variational data assimilation, the random vector fields of the background wind errors are assumed to be statistically homogeneous and isotropic in the horizontal and statistically stationary in time. Under these assumptions, the observation error variance and background error covariance can be estimated from time series of radiosonde innovation (observation minus background) data by using the conventional innovation method (Hollingsworth and Lönnberg 1986; Xu et al. 2001). However, due to the limited resolution and coverage of the radiosonde observations, the estimated background error covariance structures are confined to the synoptic and subsynoptic scales.

Doppler radar observations have high spatial and temporal resolutions, but the observed velocity is limited to only a single component of the vector wind, that is, the radial component projected onto the radar beam. Under the same assumptions as mentioned above, the random scalar fields of background radial-velocity errors are not isotropic. By using the non-isotropic form of error covariance function derived for radial-velocity fields on conical surfaces of low-elevation radar scans (Xu and Gong 2003), the conventional innovation method was reformulated by Xu et al. (2007) to estimate radar radial-velocity observation error covariance and background vector wind error covariance from time series of radar radial-velocity innovation fields.

The method of Xu et al. (2007) was designed and applied to radial-velocity observations from a single Doppler radar, while the background winds were analyses of independent radial-velocity observations from another radar. When the background fields are provided by the operational model predictions, the range of the background wind error correlation is often too large to be covered by innovation data obtained from a single Doppler radar. Thus, for operational applications, the method needs to be extended and applied to multiple-radar observations. The required extension is done recently and the method is applied to innovation data produced from multiple-radar radial-velocity observations and NCEP WRF-NMM model predictions. The preliminary results are represented in this paper.

* Corresponding author address: Qin Xu, National Severe Storms Laboratory, 120 David L. Boren Blvd., Norman, OK 73072-7326; E-mail: Qin.Xu@noaa.gov

2. THE METHOD

2.1 *Basic Assumptions and Velocity Error Covariance Tensor*

As mentioned in the introduction, the random vector fields of background wind errors are traditionally assumed to be horizontally homogeneous and isotropic over local (or regional) areas in the widely used statistical interpolation and three-dimensional variational techniques for large-scale and synoptic-scale atmospheric data assimilation (see Chapters 4-5 of Daley 1991). This assumption is likely to be less valid at the mesoscale and storm-scale, but it is still adopted commonly and implicitly along with the statistical interpolation and three-dimensional variational techniques in mesoscale data assimilation. This assumption is adopted in Xu et al. (2007) while the projection of the background wind error on each conical surface of radar scans was treated approximately as a horizontal component and is denoted by $\mathbf{v}(\mathbf{x}) = (u(x, y), v(x, y))^T$ or, simply, $\mathbf{v} = (u, v)^T$ where $(\ )^T$ denotes the transpose of ( ).

The covariance function of the random vector field $\mathbf{v}(\mathbf{x})$ involves two points, say, $\mathbf{x}_i = (x_i, y_i)$ and $\mathbf{x}_j = (x_j, y_j)$ and is defined by the following second-order tensor function:

$$\mathbf{C}_{\mathbf{vv}}(\mathbf{x}_i, \mathbf{x}_j) \equiv \langle \mathbf{v}'_i \mathbf{v}'^{,T}_j \rangle, \qquad (1)$$

where $\langle(\bullet)\rangle$ denotes the expectation or statistical mean of $(\bullet)$, $\mathbf{v}'_i = \mathbf{v}_i - \langle \mathbf{v}_i \rangle$ and $\mathbf{v}_i = \mathbf{v}(\mathbf{x}_i)$. The velocity vector $\mathbf{v}'_i$ can be projected onto the l-direction along vector $\mathbf{x}_j - \mathbf{x}_i$ (from point $\mathbf{x}_i$ to point $\mathbf{x}_j$) and onto the t-direction that is perpendicular to the l-direction with positive to the left (see Fig. 1). The resulting components are denoted by l_i and t_i, respectively. These two components are related to $\mathbf{v}'_i = (u'_i, v'_i)^T$ by $(l_i, t_i)^T = \boldsymbol{R}\mathbf{v}'_i$ where $\boldsymbol{R} = \boldsymbol{R}(\alpha)$ is the rotational matrix that rotates

the x-axis to the l-direction and $\alpha \equiv \tan^{-1}[(y_j - y_i)/(x_j - x_i)]$ is the angle of the rotation, measured positively counterclockwise (see Fig. 1).

Under the assumed homogeneity and isotropy, the canonical form of the covariance tensor defined by $\boldsymbol{C} \equiv \langle l_i, t_i)(l_j, t_j)^T \rangle$ is diagonal and invariant with respect to translations and rotations of the system of points $\mathbf{x}_i$ and $\mathbf{x}_j$. This implies that $\boldsymbol{C} = \boldsymbol{C}(r) = \text{diag}[C_{ll}(r), C_{tt}(r)]$ is independent of α, where $C_{ll}(r) \equiv \langle l_i l_j \rangle$, $C_{tt}(r) \equiv \langle t_i t_j \rangle$, and $r = |\mathbf{x}_i - \mathbf{x}_j| = [(x_j - x_i)^2 + (y_j - y_i)^2]^{1/2}$ is the horizontal distance between the two points. The four component equations of $\mathbf{C_{vv}}(\mathbf{x}_i, \mathbf{x}_j) = \boldsymbol{R}(\alpha)\boldsymbol{C}(r)\boldsymbol{R}^T(\alpha)$ yield explicit expressions for the four components of $\mathbf{C_{vv}}$ [see Eq. (2.4) of Xu et al. 2007].

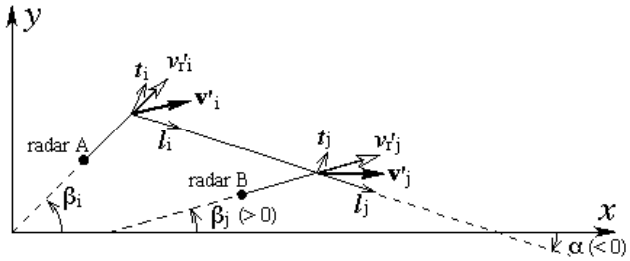

Fig. 1. Velocity vectors (bold arrows denoted by $\mathbf{v}'_i$ and $\mathbf{v}'_j$), their radial components (hollow arrows denoted by v'_{ri} and v'_{rj}), l-components (thin arrows denoted by l_i and l_j), and t-components (thin arrows denoted by t_i and t_j) at two correlated points $\mathbf{x}_i = (x_i, y_i)$ and $\mathbf{x}_j = (x_j, y_j)$. Angles α, β_i and β_j are defined in the text. The two black dots mark the locations of radar A and radar B at $\mathbf{x}_A$ and $\mathbf{x}_B$, respectively.

2.2 *Radial-velocity Error Covariance Function*

As shown in Fig. 1, with respect to radar A at $\mathbf{x}_A$, the radial component of $\mathbf{v}'_i = (u'_i, v'_i)$ at $\mathbf{x}_i$ is given by $v'_{ri} = u'_i\cos\beta_i + v'_i\sin\beta_i$ where $\beta_i = \tan^{-1}[(y_i - y_A)/(x_i - x_A)]$. Similarly, with respect to radar B at $\mathbf{x}_B$, the radial component of $\mathbf{v}'_j = (u'_j, v'_j)$ at $\mathbf{x}_j$ is given by $v'_{rj} = u'_j\cos\beta_j + v'_j\sin\beta_j$ where $\beta_j = \tan^{-1}[(y_j - y_B)/(x_j - x_B)]$. By using these expressions, the covariance function of v'_r can be obtained in the following form:

$$C_{rr} \equiv \langle v'_{ri} v'_{rj} \rangle = [C_+(r)\cos\beta_- + C_-(r)\cos\beta_+]/2. \quad (2)$$

where $C_+(r) = C_{ll}(r) + C_{tt}(r)$, $C_-(r) = C_{ll}(r) - C_{tt}(r)$, $\beta_- = \Delta\beta_i - \Delta\beta_j$, $\beta_+ = \Delta\beta_i + \Delta\beta_j$, $\Delta\beta_i = \beta_i - \alpha$ and $\Delta\beta_j = \beta_j - \alpha$. Note that $\Delta\beta_i$ (or $\Delta\beta_j$) is the angle of vector $\mathbf{x}_i$ (or $\mathbf{x}_j$) with respect to vector $\mathbf{x}_j - \mathbf{x}_i$ (measured positive counterclockwise), while $\beta_- = \Delta\beta_i - \Delta\beta_j = \beta_i - \beta_j$ is the angle of vector $\mathbf{x}_i$ with respect to vector $\mathbf{x}_j$. This result and its derivation are essentially the same as in Eq. (2.6) of Xu and Gong (2003) except that β_i and β_j are defined with respect to two different radars. If the two radial velocities at points $\mathbf{x}_i$ and $\mathbf{x}_j$ are observed by the same radar, then $\mathbf{x}_A = \mathbf{x}_B$ and the result in Eq. (2) reduces to that in Eq. (2.6) of Xu and Gong (2003). For given radars, C_{rr} depends on the function forms of $C_{ll}(r)$ and $C_{tt}(r)$. These function forms can be estimated from the partitioned innovation covariance as shown in Xu et al. (2007). The method is reviewed briefly in the next subsection.

2.3 *Innovation Covariance Partition*

In addition to the basic assumptions stated in section 2.1 for the background wind error, radar radial-velocity observation errors are assumed to be (i) not cross-correlated with background errors and (ii) not auto-correlated when $r > r_o$, where r_o is the range of observation error correlation. The second assumption should be valid as long as r_o is properly selected (based on the structure of binned innovation covariance in the vicinity of $r = 0$). This assumption considers the possible observation error correlation between neighboring or nearby beams or gates, and thus is a more relaxed condition than assumed in the conventional innovation method. As explained in the introduction of Xu et al. (2007), radar instrumentation errors may be weakly or moderately correlated between adjacent beams or adjacent gates, but the correlation decreases rapidly to near zero beyond two beams or two range gates. Radar sampling errors may be also correlated between partially overlapped radar resolution volumes. Thus, the correlation range r_o for the observation (instrumentation plus sampling) error could be several times as large as the beam width or range gate distance.

With the above assumptions, the innovation correlation (that is, the normalized innovation covariance) can be partitioned as follows

$$\langle d_i d_j \rangle = \begin{cases} C_{rr}/\sigma_d^2 & \text{for } r \ge r_o \\ (C_{rr} + C_{rr}^o)/\sigma_d^2 & \text{for } 0 \le r < r_o, \end{cases} \quad (3)$$

where $d_i = (v_{rdi} - \langle v_{rdi} \rangle)/\sigma_{di}$ is the normalized innovation at the i-th observation point $\mathbf{x}_i$, $v_{rdi} = v_{roi} - v_{rbi}$ is the innovation obtained by subtracting the background radial wind v_{rbi} from the observed radial velocity v_{roi} at the i-th observation point, $\sigma_{di}^2 = \langle (v_{rdi} - \langle v_{rdi} \rangle)^2 \rangle$ is the innovation variance computed at the i-th observation point, σ_d^2 is the averaged innovation variance computed from σ_{di}^2 over all observation points, and C_{rr}^o denotes the radar radial-velocity

observation error covariance. The statistical mean on the left-hand side of Eq. (3) is given by the time mean computed from the time series of the normalized innovations for each qualified pair of observation points. (A pair is qualified only if the time series of $d_i d_j$ covers at least 60% of the total 55 time levels).

The background error covariance C_{rr} in Eq. (3) is modeled by Eq. (2) with $C_+(r)$ and $C_-(r)$ expressed by truncated spectral expansions [see Eq. (3.2) of Xu et al. 2007]. According to Eq. (3), $C_+(r)$ and $C_-(r)$ can be estimated by fitting the spectral expansion of C_{rr}/σ_d^2 to the innovation correlation $<d_i d_j>$ over the range of $r_o \le r \le D$ where D is the maximum range of background error correlation. For the background fields produced by analyses of independent observations from another radar in Xu et al. (2007), D is about 50 km and can be covered by innovation data obtained from a single radar. In this study, the background fields are provided by WRF-NMM model predictions, so D is much larger than 50 km and cannot be covered by single-radar innovation data. Because of this, radial-velocity innovation data are collected from six radars to estimate the background wind error covariance in this study.

As shown in Eq. (4.1) of Xu et al. (2007), C_{rr} in Eq. (2) reduces approximated to a quadratic function of r in the small-scale range ($r \le 10$ km). By fitting this quadratic function to innovation correlation data obtained from a single Doppler radar over the small-scale range of $r_o \le r \le 10$ km, the background error variance can be estimated by extrapolating the quadratic function from $r = r_o$ to $r = 0$, and then the observation error variance can be estimated by subtracting the background error variance from the innovation variance according to Eq. (3). The residuals of the fitting (obtained by subtracting C_{rr}/σ_d^2 from the innovation correlation) can be used to estimate the observation error covariance C_{rr}^o over the unfitted range of $0 \le r \le r_o$ according to Eq. (3). The observation error covariance function C_{rr}^o can be modeled similarly as the background error covariance C_{rr}, but the spectral expansions should now represent $C_+^o(r)$ and $C_-^o(r)$ and thus diminish rapidly as r increases toward r_o. In other words, $C_+^o(r)$ and $C_-^o(r)$ should be compactly supported and confined within the range of $0 \le r \le r_o$ (instead of $0 \le r \le D$).

3. INNOVATION DATA

3.1 *Observation and Background Data*

The radial-velocity observations used in this study were collected from six radars (KINX, KLZK, KSGF, KSRX, KTLX and KVNX as shown in Fig. 2) on 05/21/2005 under a clear but windy weather condition. Each radar scanned roughly every 10 minutes per volume with radial-velocity data collected at high spatial resolutions: 0.25 km in the radial direction and near 1° in the azimuthal direction. Technically the radial range coverage is 230 km for each radar, but significant echoes and radial-velocity measurements were available mainly within 100 km even for scans at the lowest elevation angle (= 0.5°) from each radar (see Fig. 2). Under such a clear weather condition, the data coverage reduces rapidly as the elevation angle increases. The scans used in this study are thus limited to the five lowest elevation angles (that is, 0.5, 1.5, 2.5, 3.5 and 4.5 degree for most cases). Since migrating-bird contaminations are detected for the nighttime scans (Zhang et al. 2005; Liu et al. 2005), only daytime scans (from 13:00 to 24:00 UTC) are used. After dealiasing (Gong et al. 2003) and quality control, radial-velocity volume scans are selected at 55 time levels.

The background wind fields were provided by WRF-NMM 3-hour forecasts on a 321x321x61 E-grid with a sigma vertical coordinate and 8 km horizontal resolution over the central US. The background wind fields are interpolated onto 55 time levels in synchronization approximately with the radial-velocity volume scans from the six radars. The synchronized background vector winds are then interpolated in space to each radar observation point and projected onto the radar beam direction to obtain the background radial wind. By subtracting the synchronized and interpolated background radial wind from their respective observations in the observation space, radial-velocity innovation data are generated at the 55 time levels in the three-dimensional space covered by volume scans from the six radars.

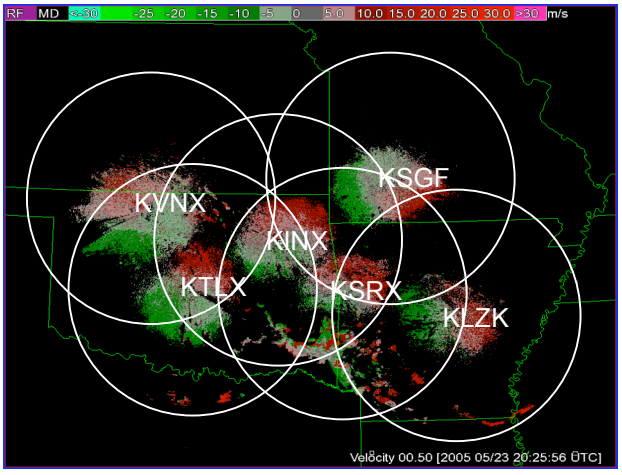

Fig. 2. Sampled radial-velocity images at 0.5° elevation angle from the six radars (KINX, KLZK, KSGF, KSRX, KTLX and KVNX) on 05/21/2005. The circles show 250 km range rings from each of the six radars.

3.2 *Innovation Correlation Data Binning*

The innovation data are confined in vertical between z = 0.2 and 2.2 km. This depth is equally divided into five contiguous layers centered at z = 0.4, 0.8, 1.2, 1.6 and 2 km, respectively, above the ground level. Within each layer, the statistical mean of $d_i d_j$, that is, $<d_i d_j>$ on the left-hand side of Eq. (3) is computed as the time mean of $d_i d_j$ for each qualified ij-pair of observation points. A ij-pair is qualified only if the time series of $d_i d_j$ cover at least 60% of the total 55 time levels. The computed innovation correlation data clouds are then binned every 0.25 km in r, every ±0.1 for $|\cos\beta_-| < 0.9$ and $|\cos\beta_+| \le 0.9$, and every 0.1 for $0.9 \le |\cos\beta_-| \le 1$ and $0.9 \le |\cos\beta_+| \le 1$. The lowest layer ($z$ = 0.4 ± 0.2 km) has the largest number of qualified pairs. The number of qualified pairs in each bin box in this lowest layer is plotted as discrete functions of r in Fig. 3 for three sets of bin intervals in the vicinities of (i) $\cos\beta_-$ = 1 and $\cos\beta_+$ = 1, (ii) $\cos\beta_-$ = 1 and $\cos\beta_+$ = 0, and (iii) $\cos\beta_-$ = 1 and $\cos\beta_+$ = -1. The innovation correlation (averaged in each bin box) is plotted as discrete functions of r in Fig. 4 for the same three sets of $\cos\beta_-$ and $\cos\beta_+$ as in Fig. 3.

As shown in Figs. 3 and 4, there is no qualified innovation data pair over the middle range between 40 < r < 110 km. Over the far range between 100 < r < 250 km, all the innovation pairs are formed by observations from two different radars and the number of qualified pairs in a bin box can rarely exceed 5000. Over the near range of r < 40 km, the innovation pairs are formed by observations from a single radar and the number of qualified pairs in a bin box can be very large (occasionally even beyond the plotted range 60000).

4. ESTIMATED ERROR STATISTICS

4.1 *Background Error Covariance*

The background wind error covariance functions $C_+(r)$ and $C_-(r)$ can be estimated for each layer by the two-step fitting method of Xu et al. (2007). In the first step, the background (component) wind error variance (denoted by σ^2) is estimated as the value of C_{rr} at r = 0 by fitting the quadratic-function form of C_{rr}/σ_d^2 to the binned innovation correlation data points over the range of 10 km ≥ r ≥ r_o (= 2 km) according to Eq. (3). In the second step, the truncated spectral expansions of $C_+(r)$ and $C_-(r)$ are estimated by fitting C_{rr}/σ_d^2 to the binned innovation correlation data points over the range of $r_o \le r \le$ 250 km according to Eqs. (2) and (3). However, due to the general lack of qualified pairs over the far range, all the binned innovation correlation data are used in the fitting in this study.

Three fitted curves of C_{rr}/σ_d^2 are plotted in Fig. 4 for the three sets of $\cos\beta_-$ and $\cos\beta_+$. As shown, the three curves follow the innovation correlation data reasonably well, although the accuracy of the estimated functions may be adversely affected by the absence of qualified pairs over the middle range. As the vertical layer goes higher from z = 0.4 ± 0.2 km to z = 0.8, 1.2, 1.6 and 2 ± 0.2km, the lack of qualified pairs becomes more serious and the estimate appears to be less accurate (not shown). To alleviate this problem, more qualified innovation data need to be sampled over longer time period in future studies. Nevertheless, the intercept point of the fitted curves of C_{rr}/σ_d^2 at r = 0 in Fig. 4 appears to yield a reasonably good estimate of σ^2/σ_d^2 (≈ 0.27).

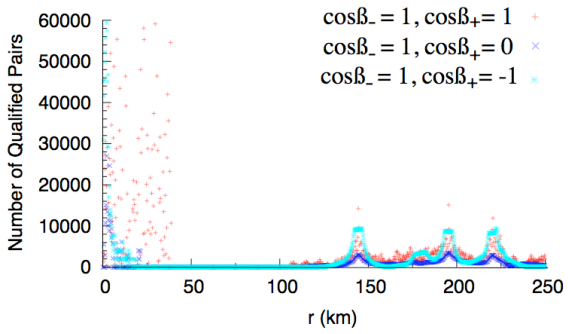

Fig. 3. Number of qualified pairs in each bin box over the range of 0 ≤ r ≤ 250 km for three sets of bin intervals in the vicinities of (i) $\cos\beta_-$ = 1 and $\cos\beta_+$ = 1, (ii) $\cos\beta_-$ = 1 and $\cos\beta_+$ = 0, and (iii) $\cos\beta_-$ = 1 and $\cos\beta_+$ = -1 in the lowest layer (z = 0.4 ± 0.2 km).

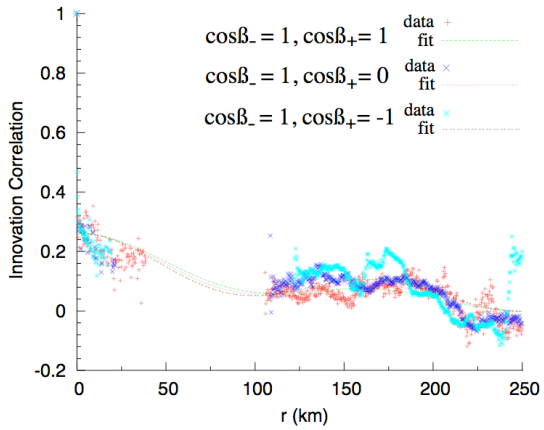

Fig. 4. Binned innovation correlation data points over the range of 0 ≤ r ≤ 250 km for the same three sets of $\cos\beta_-$ and $\cos\beta+$ bin intervals as in Fig. 3. Three fitted curves of C_{rr}/σ_d^2 are plotted for the three sets of $\cos\beta_-$ and $\cos\beta_+$.

The estimated background error correlation functions in the lowest layer are plotted in Fig. 5, where $R_+(r) \equiv C_+(r)/C_+(0)$, $R_-(r) \equiv C_-(r)/C_+(0)$, and $C_+(0) = 2\sigma^2$ is the background vector wind error variance. According to Eqs. (4.4)-(4.5) of Xu and Wei (2001), the estimated covariance function $C_+(r)$ can be partitioned into three parts, that is,

$$C_+(r) = C_0 + C_{\text{div}}(r) + C_{\text{rot}}(r), \qquad (4)$$

where C_0 is the unresolved large-scale part, $C_{\text{div}}(r)$ is the divergent part, $C_{\text{rot}}(r)$ is the rotational part. The correlation function $R_+(r)$ can be partitioned in the same way. Here, for simplicity, we can further and equally partition C_0 and thus define the divergent and rotational parts of the correlation function by $R_{\text{div}} \equiv [C_0/2 + C_{\text{div}}(r)]/C_+(0)$ and $R_{\text{rot}} \equiv [C_0/2 + C_{\text{rot}}(r)]/C_+(0)$, respectively. As shown in Fig. 5, the estimated R_{div} and R_{rot} have similar shape but slightly different amplitudes. The amplitude of R_{div} is slightly larger than that of R_{rot}, and this feature is dynamically consistent with the enhanced flow divergence in the boundary layer.

4.2 *Refined Error Variance Estimation*

As shown in Fig. 4, the innovation correlation data points increase rapidly towards 1 at $r = 0$. These rapid increases are caused by correlated observation errors within the range of $r < r_o$ according to Eq. (3). By setting $r = 0$ in Eq. (3), we have $C_{rr}^o(0) = \sigma_o^2 = \sigma_d^2 - \sigma^2$, so the radar radial-velocity observation error variance σ_o^2 can be estimated by subtracting the estimated background error variance σ^2 from the innovation variance σ_d^2. The estimated σ_o^2, however, is an averaged observation error variance for the six radars, although the same procedure was used in Xu et al. (2007) to estimate σ_o^2 for single-radar radial-velocity observations at the lowest tilt.

In this section, the above procedure is applied to innovation data collected separately from each radar in each vertical layer. In this case, the innovation correlation data binning strategy can be refined and made simpler and more efficient than that used in section 4.1 (and in Xu et al. 2007). Note that a set of innovation data collected in a selected vertical layer from single-radar scans at a selected tilt is confined in a circular area (between two circles) on the selected tilt. In our case, each set of innovation data collected from single-radar scans at the 5 lowest tilts is confined in 5 circular areas in each selected layer. Such a set of innovation data can be simply paired for short separations in only two directions; that is, (i) the radial direction along each radar beam with $r \le 10$ km and (ii) the azimuthal direction along each range circle with $|\beta_-| \le 10^o$, where β_- is defined Eq. (2). For short separations (with $r \le 10$ km or $|\beta_-| \le 10^o$), the binned innovation correlation patterns in these two directions can be expressed by $[C_{ll} + C_{ll}^o]/\sigma_d^2$ and $[C_{tt} + C_{tt}^o]/\sigma_d^2$, respectively. Here, as explained in section 2.3, the background covariance functions C_{ll} and C_{tt} can be modeled by quadratic functions of r and $|\beta_-|$, respectively.

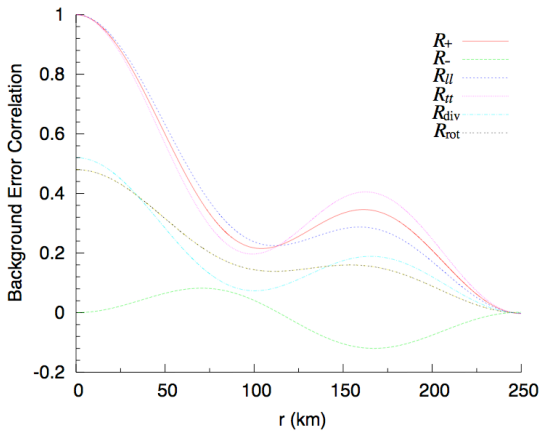

Fig. 5. Estimated background wind error correlation functions in the lowest layer ($z = 0.4 \pm 0.2$ km).

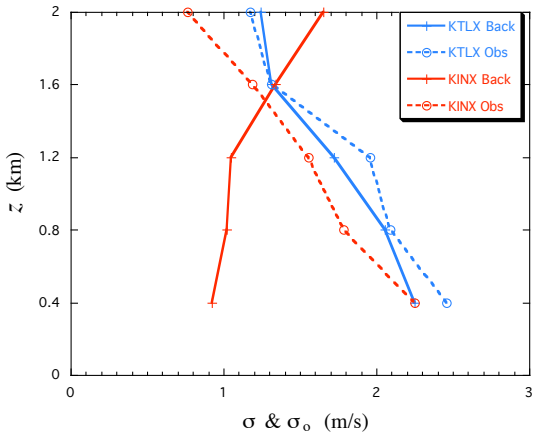

Fig. 6. Estimated vertical profiles of σ (solid) and σ_o (dashed) over KTLX (in blue) and KINX (in red).

With the above refinements, the background and observation variances can by estimated efficiently in using only the first step of the two-step fitting method mentioned in section 4.1. Examples of the estimated σ and σ_o are plotted as functions of height (over the five vertical layers) for KTLX and KINX radars in Fig. 6. As shown, the two radars have roughly the same

vertical profile of σ_o, but the background winds have quite different vertical profiles of σ above the two radars.

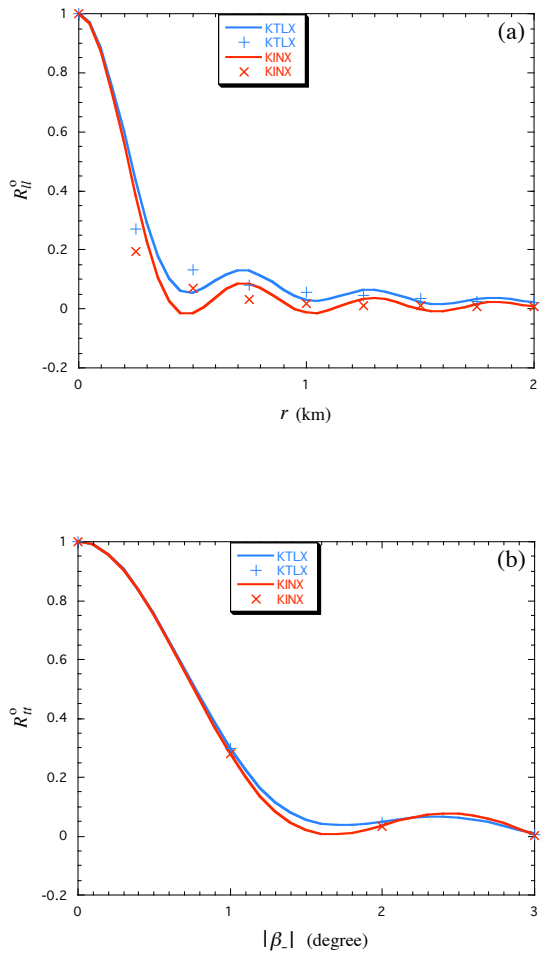

Fig. 6. Estimated (a) $R_{ll}^o(r)$ and (b) $R_{tt}^o(|\beta\_|)$ for KTLX (in blue) and KINX (in red) observations in the lowest layer. Symbols + and × show the rescaled data from KTLX and KINX, respectively.

4.3 *Observation Error Correlation*

By subtracting the estimated quadratic-function values of C_{ll}/σ_d^2 and C_{tt}/σ_d^2 from their respective innovation correlation data binned in the radial and azimuthal directions, we can obtain binned data for C_{ll}^o/σ_d^2 and C_{tt}^o/σ_d^2, respectively. These binned data can be re-scaled by σ_o^2 to yield binned data for $R_{ll}^o(r) \equiv C_{ll}^o(r)/\sigma_o^2$ and $R_{tt}^o(|\beta\_|) \equiv C_{tt}^o(|\beta\_|)/\sigma_o^2$, respectively. Here, by definition, $R_{ll}^o(r)$ is the observation error correlation between neighboring gates on the same beam and $R_{tt}^o(|\beta\_|)$ is the observation error correlation between neighboring beams on the same range circle. As explained in section 2.3, the $R_{ll}^o(r)$ and $R_{tt}^o(|\beta\_|)$ can be modeled by spectral expansions within the ranges of $0 \le r \le r_o$ (= 2 km) and $0 \le |\beta\_| \le \beta_o$ (= 3°), respectively.

The estimated function forms of $R_{ll}^o(r)$ for KTLX and KINX observations in the lowest layer are plotted along with their fitted rescaled data in Fig. 7a. As shown, the estimated function forms of $R_{ll}^o(r)$ are similar for the two radars, although the small-amplitude oscillations in these functions appear to be spurious miss-fittings (caused by spectral truncations). The estimated function forms of $R_{tt}^o(|\beta\_|)$ for KTLX and KINX observations in the lowest layer are plotted along with their fitted rescaled data in Fig. 7b. As shown, the estimated function forms of $R_{tt}^o(|\beta\_|)$ are nearly identical for the two radars, and they both fit their respective rescaled data very closely.

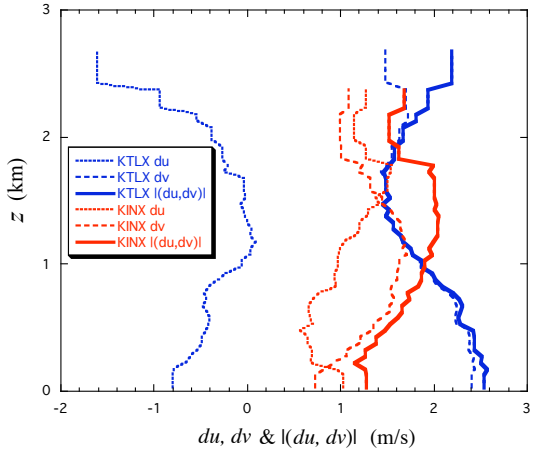

Fig. 8. Vertical profiles of estimated du, dv and $|(du, dv)|$ over KTLX and KINX areas, where (du,dv) denotes the (observation minus background) wind bias difference .

4.4 *Bias Difference Estimation*

When the normalized radial-velocity innovation is computed in Eq. (3), the innovation mean is subtracted from the innovation at each observation point. By definition, the radial-velocity innovation mean at the i-th observation point is given by $\langle v_{rdi} \rangle = \langle v_{roi} \rangle - \langle v_{rbi} \rangle$, where $\langle v_{roi} \rangle$ is the radial-velocity observation bias and $\langle v_{rbi} \rangle$ is the radial-velocity background bias at the i-th observation point. By using the (modified and classic) combined VAD method of Gong et al (2003), the radial-velocity innovation mean field from each radar can be used to estimate the bias difference between the

observation-estimated horizontal (vector) wind and background horizontal wind at each vertical level. The estimated bias differences are plotted as functions of height for KTLX and KINX radars in Fig. 8. As shown, the vector bias differences are quite different over the two radars but their absolute values have the same order of magnitude as the estimated observation and background error standard deviations (see Fig. 6).

5. CONCLUSIONS

In this paper, the method of Xu et al. (2007) is extended and used to estimate the averaged radar radial-velocity observation error variance and background wind error covariance from radial-velocity innovation data collected from six radars during the daytime period on 05/21/2005 under a clear but windy weather condition. The background wind fields were provided by WRF-NMM 3-hour forecasts (on a 321x161x61 E-grid with a sigma vertical coordinate and 8 km horizontal resolution) over the central US. The results show that the observation and background) error variances can be reasonably well estimated along with the background wind error correlation functions in the boundary layer, although the accuracy of the estimated correlation functions may be adversely affected by the lack of qualified innovation data for the middle-range separations (between $40 < r < 110$ km for the lowest layer within $z = 0.4 \pm 0.2$ km). To alleviate the problem caused by insufficient data coverage, additional innovation data need to be collected (over multiple days) and used in future studies.

The method is also refined to estimate the radial-velocity observation error correlation functions and the vertical profiles of observation and background error standard deviations over each radar area. The estimated vertical profiles show that the radial-velocity observation errors are about the same (≈ 2 m s^{-1}) for different radars and decrease generally with height in the boundary layer. The background wind error is also about 2 m s^{-1} but have different vertical variations at different radar areas. The estimated observation error correlation functions have similar shapes for different radars, and they all show that radar radial-velocity observation errors are correlated in two different ways between neighboring range gates and between neighboring beams.

Observation-minus-background (vector) wind bias difference is estimated as a function of height over each radar area. The estimated bias differences are significantly different over different radar areas. Their absolute values have the same order of magnitude as the estimated observation and background error standard deviations. How to estimate the observation and background biases based on the estimated bias differences is an unresolved problem and requires more studies with additional assumptions.

Acknowledgements. The research was supported by the ONR Grant N000140410312 to the University of Oklahoma and by FAA contract IA# DTFA03-01-X-9007 and NOAA HPCC program to NSSL. Funding was also provided to CIMMS by NOAA/Office of Oceanic and Atmospheric Research under NOAA-University of Oklahoma Cooperative Agreement #NA17RJ1227, Department of Commerce.

REFERENCES

Daley, R. 1991: *Atmospheric Data Analysis*. Cambridge University Press, 457 pp.

Gong, J., Wang L. and Xu, Q. 2003: A three-step dealiasing method for Doppler velocity data quality control. *J. Atmos. & Oceanic Technol.*, **20**, 1738-1748.

Hollingsworth, A. and Lönnberg, P. 1986: The statistical structure of short-range forecast errors as determined from radiosonde data. Part I: The wind field. *Tellus*, **38A**, 111–136.

Liu, S., Xu, Q. and Zhang, P. 2005: Quality control of Doppler velocities contaminated by migrating birds. Part II: Bayes identification and probability tests. *J. Atmos. Oceanic Technol.* **22**, 1114-1121.

Xu, Q. and Gong, J. 2003: Background error covariance functions for Doppler radial-wind analysis. *Q. J. R. Meteorol. Soc.*, **129**, 1703-1720.

Xu, Q., K. Nai, and L. Wei, 2007: An innovation method for estimating radar radial-velocity observation error and background wind error covariances. *Quart. J. Roy. Meteor. Soc.*, **133**, 407-415.

Xu, Q. and Wei, L. 2001: Estimation of three-dimensional error covariances. Part II: Analysis of wind innovation vectors. *Mon. Weather Rev.*, **129**, 2939-2954.

Xu, Q., Wei, L., VanTuyl A. and Barker, E. H. 2001: Estimation of three-dimensional error covariances. Part I: Analysis of height innovation vectors. *Mon. Weather Rev.*, **129**, 2126–2135.

Zhang, P., Liu, S. and Xu, Q. 2005: Quality control of Doppler velocities contaminated by migrating birds. Part I: Feature extraction and quality control parameters. *J. Atmos. Oceanic Technol.*, **22**, 1105-1113.